Modelling the anisotropic inelastic response of polymeric scaffolds for in situ tissue engineering applications

Michele Terzano[a], Maximilian P. Wollner[a], Manuel P. Kainz[a], Malte Rolf-Pissarczyk[a], Nils Götzen[b], Gerhard A. Holzapfel[a,c,*]

[a]*Institute of Biomechanics, Graz University of Technology, Graz, Austria*
[b]*4RealSim Services BV, IJsselstein, The Netherlands*
[c]*Department of Structural Engineering, Norwegian University of Science and Technology (NTNU), Trondheim, Norway*

Abstract

In situ tissue engineering offers an innovative solution for replacement valves and grafts in cardiovascular medicine. In this approach, a scaffold, which can be obtained by polymer electrospinning, is implanted into the human body and then infiltrated by cells, eventually replacing the scaffold with native tissue. *In silico* simulations of the whole process in patient-specific models, including implantation, growth and degradation, are very attractive in order to study the factors that might influence the end result. In our research we focused on the mechanical behavior of the polymeric scaffold and its short-term response. Following a recently proposed constitutive model for the anisotropic inelastic behavior of fibrous polymeric materials, we present here its numerical implementation in a finite element framework. The numerical model is developed as user material for commercial finite element software. The verification of the implementation is performed for elementary deformations. Furthermore, a parallel plate test is proposed as a large-scale representative example and the model is validated by comparison with experiments.

Keywords:
Tissue engineering, endogenous tissue restoration, electrospinning, anisotropy, viscoelasticity

1. Introduction

Cardiovascular diseases, which affect the heart and blood vessels, remain the leading cause of death worldwide. In particular, the aortic valve, which connects the aorta with the left ventricle and prevents backflow of blood into the heart during diastole, may be affected by valve stenosis and regurgitation [1]. Today, these pathological conditions are often treated with a minimally

*Corresponding author. E-mail: holzapfel@tugraz.at

invasive surgical procedure called transcatheter aortic valve implantation (TAVI), in which a replacement heart valve is positioned through a catheter [2]. The most common solutions include mechanical and bioprosthetic heart valves manufactured from processed animal tissue. However, both categories have several drawbacks, including poor biocompatibility and age-related structural deterioration [3]. Innovative solutions are made available through *in situ* tissue engineering, also known as endogenous tissue restoration (ETR), in which a temporary bioabsorbable polymeric scaffold provides the biomechanical structural characteristics until the native tissue is produced [4–8]. In addition to heart valves, ETR is a promising technique for replacement vascular grafts [9, 10]. The key benefits of such an approach are that it avoids the long-term presence of foreign materials in the body, provides a replacement heart valve with a native-like response to hemodynamic loads, and has the ability to remodel and regenerate [4].

Cardiovascular tissues appear as sophisticated assemblies of fibres and cells that respond to a range of biomechanical and biochemical stimuli and can adapt to physiological and pathological conditions [11]. Therefore, the design of functional heart valves is a complex task that requires knowledge of the structural and mechanical characteristic of the native tissue as well as the biomechanical loads *in vivo* [12]. Furthermore, the success of ETR depends on the cellular response to the scaffold, e.g., with regard to infiltration, adhesion, and immunogenic response [8]. In terms of mechanical behavior, heart valves require excellent fatigue resistance to continuous exposure from cyclic pressures, shear stresses, and strains resulting from hemodynamic loads [4]. In this context, the amount and spatial arrangement of collagen fibres is of fundamental importance, and it has been observed that the formation and organisation of restored native tissue can be controlled by incorporating anisotropy into the scaffold [13]. In addition, fibre diameter and alignment correlate with pore size and thus have a direct influence on cell infiltration [14]. Synthetic polymers produced by electrospinning are among the most promising materials for biodegradable scaffolds with non-woven meshes featuring micrometer-sized fibres [15, 16].

Given the large number of variables involved in tissue engineering design, simulation-based methods are highly attractive [17–19]. Computational tools allow the prediction of the entire ETR process. However, the accuracy of their results is highly dependent on constitutive models used to describe the short-term mechanical response of the biodegradable scaffold, its interaction with the hemodynamic environment, the process of cell infiltration and growth of native tissue, and finally the scaffold degradation [20–23]. The mechanical behavior of the scaffold is similar to

other fibre–reinforced soft composites, including biological tissues [24], textiles [25], fibre-reinforced polymers [26] and biopolymer gels [27]. These materials are endowed with peculiar features that are a direct expression of the arrangement of their microstructure and the interactions within it. More specifically, the mechanical response of electrospun polymeric meshes is characterised by large deformations, nonlinearity, and anisotropy [14, 28, 29]. In addition, numerous inelastic effects are also observed in the experiments, including stress-softening, permanent deformation, and rate-dependence [30]. In fact, these features are also found in vascular tissues. For example, rate-dependence is particularly relevant for the aortic valve, which *in vivo* is subject to high deformation rates [31].

Here we present a computational model to describe the short-term inelastic response of polymeric scaffolds for tissue engineering applications. The constitutive framework is based on a recently formulated continuum mechanics approach that combines anisotropy, stress-softening, permanent deformations, and rate-dependency [32]. This base model served as the foundation for modelling the ETR process in a biodegradable scaffold embedded in a thorough verification, validation, and uncertainty quantification plan [33, 34], as developed in the Horizon 2020 Project of the European Union *SimInSitu*. Aiming to simulate the entire ETR process, fluid-structure interaction, growth and remodelling, and patient-specific geometry, an efficient numerical implementation in industry-standard finite element (FE) codes is a key goal of this research. Hence, we derive simple algorithmic expressions for the computation of the spatial stress tensor and the consistent tangent modulus needed for standard implementations in implicit solvers developed in the updated-Lagrangian formulation. The FE code verification is performed by comparing the implementation in user-material subroutines for the commercial Abaqus software [35] with analytical solutions for elementary deformations. We also consider a large scale representative example consisting of the simulation of a parallel-plate compression test with cyclic loading. In particular, we describe the experimental procedure for the mechanical characterisation of the electrospun polymeric scaffold and use FE simulation to validate the proposed computational model.

2. Computational model

2.1. Constitutive modelling framework

The constitutive model for the scaffold material is developed within finite strain continuum mechanics and irreversible thermodynamic with internal variables, and includes anisotropic hy-

perelastic response, stress-softening, permanent deformation, and rate-dependence. The reader is referred to the authors' recent work [32] for a detailed presentation and background of the thermodynamic principles involved. Here we summarise the main features of the proposed approach:

- According to Simo [36] and Holzapfel *et al.* [37], a free-energy function is introduced as the sum of an equilibrium part Ψ^{∞} and a non-equilibrium part $\sum_{l=1}^{M}\Upsilon_l$, where each term Υ_l is responsible for a viscoelastic contribution. Furthermore, the canonical volumetric-isochoric multiplicative split of the deformation gradient $\mathbf{F}$ is used [38], $\mathbf{F}=(J^{1/3}\mathbf{I})\overline{\mathbf{F}}$, where $J=\det\mathbf{F}>0$, leading to an additive form of the free energy. The split is also consistent with the observation that viscous effects on the volumetric behavior are negligible, so the non-equilibrium part is treated as purely distortional [39]. The general form of the proposed free energy is [32]

$$\Psi=\Psi^{\infty}_{\mathrm{vol}}(J)+\Psi^{\infty}_{\mathrm{iso}}(\overline{\mathbf{C}})+\sum_{l=1}^{M}\Upsilon_l(\overline{\mathbf{C}},\mathbf{\Gamma}_l), \tag{1}$$

  where $\overline{\mathbf{C}}=\overline{\mathbf{F}}^{\mathrm{T}}\overline{\mathbf{F}}$ is the isochoric right Cauchy-Green tensor, $\mathbf{\Gamma}_l$ are tensorial right Cauchy-Green-like internal variables, and $\Psi^{\infty}_{\mathrm{vol}}$ is a generic convex function of the volume ratio J. The explicit form of the non-equilibrium term appearing in (1) is given in our related paper [32, Eq. (55)].

- The equilibrium part describes the time-independent material response, and we assume that it includes dissipative effects resulting in stress-softening (Mullins effect) and permanent deformation. In contrast to other works, see, e.g., [36, 40], we adopt here the pseudo-elastic model introduced by Ogden and Roxburgh [41] with its latest modifications [42]. We introduce a pair of scalar damage functions that scale the stress response depending on the maximum isochoric strain energy $\Psi^{\max}_{\mathrm{iso}}$ attained by the material during the loading history. Specifically, the general expression of this function is [32, Eq. (29)]

$$\eta(\chi;\eta_0,\eta_1,\alpha)=\eta_0+(\eta_1-\eta_0)[(\alpha+1)\chi^{\alpha}-\alpha\chi^{\alpha+1}], \tag{2}$$

  where η_0,η_1,α are different sets of parameters for stress-softening and permanent deformation, and $\chi=\Psi^{0,\infty}_{\mathrm{iso}}/\Psi^{\max}_{\mathrm{iso}}$, with $\Psi^{0,\infty}_{\mathrm{iso}}$ representing the purely elastic free energy in the undamaged material.

- The elastic response is described here by an anisotropic strain-energy function, which is part

of a large class of polyconvex constitutive relations [43]. Anisotropy is introduced by a pair of interdependent second-order symmetric structure tensors that describe the coaxial and perpendicular behavior of the material with respect to the fibres. The coaxial structure tensor is defined as $\mathbf{H}_{\parallel} = H_i \boldsymbol{E}_i \otimes \boldsymbol{E}_i$ ($i = 1, 2, 3$, summation rule applies), with $\mathbf{H}_{\parallel} : \mathbf{I} = 1$, and the perpendicular structure tensor follows in the form $\mathbf{H}_{\perp} = \frac{1}{2}(\mathbf{I} - \mathbf{H}_{\parallel})$. The orthogonal eigenvector basis $(\boldsymbol{E}_i)_{i=1}^{3}$, defines the planes of material symmetry in the reference configuration. The proposed isochoric strain-energy function is [32, Eq. (9)]

$$\Psi_{\mathrm{iso}}^{0,\infty} = \sum_{p\in\{\parallel,\perp\}} \frac{\mu_p}{2} \left\{ \frac{1}{(\gamma_p + 1)} \left[\left(\overline{K}_{1p}\right)^{\gamma_p+1} - 1 \right] + \frac{1}{(\delta_p + 1)} \left[\left(\overline{K}_{-1p}\right)^{\delta_p+1} - 1 \right] \right\}, \tag{3}$$

where $\overline{K}_{1p} = \mathbf{H}_p : \overline{\mathbf{C}}$ and $\overline{K}_{-1p} = \mathbf{H}_p : \overline{\mathbf{C}}^{-1}$ are four anisotropic isochoric invariants, capturing the isochoric deformation of line and area elements, respectively. In (3) we have introduced stiffness-like parameters $\mu_{\parallel}$ and $\mu_{\perp}$ which weight the coaxial and perpendicular contributions, respectively. In addition, four shape parameters $\gamma_{\parallel}, \gamma_{\perp}, \delta_{\parallel}$, and $\delta_{\perp}$ control the influence of the associated invariants. For example, the shape parameter γ_p can be tuned to adjust the strain-stiffening response of the material under tension, while δ_p models a decrease in stiffness [32, Fig. (2)].

Following a standard Coleman-Noll procedure [38], one obtains the second Piola-Kirchoff stress tensor additively as

$$\mathbf{S} = \mathbf{S}_{\mathrm{vol}}^{0,\infty} + J^{-2/3}\mathbb{P} : (\overline{\mathbf{S}}^{\infty} + \overline{\mathbf{S}}^{\mathrm{neq}}), \tag{4}$$

where $\mathbf{S}_{\mathrm{vol}}^{0,\infty} = p\mathbf{C}^{-1}$, with $p = \mathrm{d}\Psi_{\mathrm{vol}}/\mathrm{d}J$, and $\mathbb{P}$ is the fourth-order material projection tensor [38]. The fictitious equilibrium stress tensor $\overline{\mathbf{S}}^{\infty}$ related to the unimodular part of the deformation gradient is expressed by [32, Eq. (15), Eq. (35)]

$$\overline{\mathbf{S}}^{\infty} = \left(\eta_{\mathrm{m}}\overline{\mathbf{S}}^{0,\infty} + \eta_{\mathrm{r}}\overline{\mathbf{S}}^{\mathrm{r},\infty}\right) \quad \text{with} \quad \overline{\mathbf{S}}^{0,\infty} = 2\frac{\partial \Psi_{\mathrm{iso}}^{0,\infty}}{\partial \overline{\mathbf{C}}}, \tag{5}$$

where the damage functions $\eta_{\mathrm{m}}, \eta_{\mathrm{r}}$ follow from (2), specialised for stress-softening and permanent deformation. The effect of the permanent deformation appears in the model through residual stresses $\overline{\mathbf{S}}^{\mathrm{r},\infty} = -\overline{\mathbf{S}}^{0,\infty}(\overline{\mathbf{C}}^{\star})$, determined by the fictitious stress tensor at the instance when the

maximum isochoric free-energy function is reached [32, Sect. (5)], i.e.

$$\overline{\mathbf{C}}^{\star}(t) = \overline{\mathbf{C}}(\tau^{\star}), \quad \tau^{\star} = \arg\max_{\tau \leq t} \Psi_{\text{iso}}^{0,\infty}(\tau).$$

Furthermore, the non-equilibrium term can be written as [32, Eq. (61)]

$$\overline{\mathbf{S}}^{\text{neq}} = 2\frac{\partial^2 \Psi_{\text{iso}}^{0,\infty}}{\partial \overline{\mathbf{C}} \partial \overline{\mathbf{C}}} : \mathbf{Q} \quad \text{with} \quad \mathbf{Q} = \sum_{l=1}^{M} \mu_l'^{-1} \mathbf{Q}_l, \tag{6}$$

where the viscous overstress of each relaxation process is $\mathbf{Q}_l = \overline{\mathbf{S}}^{0,\infty} - \mu_l'(\mathbf{\Gamma}_l - \mathbf{I})$. Finally, the evolution of the viscoelastic process is prescribed by the following set of linear differential equations

$$\dot{\mathbf{Q}}_l + \frac{\mathbf{Q}_l}{\tau_l} = \dot{\overline{\mathbf{S}}}^{0,\infty}, \tag{7}$$

ensuring positive internal energy dissipation. In (6)-(7), τ_l and μ_l' are additional pairs of parameters that are introduced for each relaxation process. The strain-energy factor introduced in Wollner et al. [32, Eq. (59)] on the right-hand side of (7) is assumed here to be one without loss of generality. It is worth noting that while the internal variables appearing in the free energy (1) are right Cauchy-Green-like quantities, the evolution equation (7) is completely defined by the viscous overstress $\mathbf{Q}_l$. This structure of the evolution equation is a peculiarity of the approach derived from Simo [36] and greatly simplifies the numerical implementation, as detailed below.

2.2. Numerical implementation

2.2.1. Algorithmic stress tensor and tangent modulus

The implementation of an inelastic material model into a FE code requires an algorithmic update of the stress tensor. Following Holzapfel *et al.* [37], the closed-form solution of the evolution equations (7) is approximated by the mid-point rule, which results in

$$\mathbf{Q}_l^{(n+1)} = \mathcal{H}_l^{(n)} + \exp\left(-\frac{\Delta t^{(n+1)}}{2\tau_l}\right) \overline{\mathbf{S}}^{0,\infty\,(n+1)}, \tag{8}$$

where the superscripts $n, n+1$ are related to the time instants $t^{(n)}, t^{(n+1)}$, with $\Delta t^{(n+1)} = t^{(n+1)} - t^{(n)}$. The history terms $\mathcal{H}_l^{(n)}$ are tensorial quantities defined by

$$\mathcal{H}_l^{(n)} = \exp\left(-\frac{\Delta t^{(n)}}{2\tau_l}\right) \left[\exp\left(-\frac{\Delta t^{(n)}}{2\tau_l}\right) \mathbf{Q}_l^{(n)} - \overline{\mathbf{S}}^{0,\infty\,(n)}\right]. \tag{9}$$

The steps needed to obtain the total Eulerian stress tensor are summarised in Algorithm 1.

Algorithm 1 Computation of the Eulerian stress tensor

Given $\Delta t^{(n)}, \mathbf{F}^{(n)}, \Psi_{\text{iso}}^{\max(n-1)}, \overline{\mathbf{S}}^{\text{r},\infty(n-1)}, \mathcal{H}_l^{(n-1)}$
Evaluate J, $\mathbf{C}$, $\overline{\mathbf{C}}$, $\mathbf{C}^{-1}$ and $\overline{\mathbf{C}}^{-1}$
Evaluate $\overline{K}_{1\{\|,\perp\}}$, $\overline{K}_{-1\{\|,\perp\}}$
Evaluate $\overline{\mathbf{S}}^{0,\infty}$ from (5):

$$\overline{\mathbf{S}}^{0,\infty} = \sum_{p\in\{\|,\perp\}} \mu_p \left(\overline{K}_{1p}^{\gamma_p} \mathbf{H}_p - \overline{K}_{-1p}^{\delta_p} \mathbf{H}'_p \right) , \quad \text{with :} \quad \mathbf{H}'_p = \overline{\mathbf{C}}^{-1} \mathbf{H}_p \overline{\mathbf{C}}^{-1}$$

if $\Psi_{\text{iso}}^{\max(n-1)} < \Psi_{\text{iso}}^{0,\infty}$ **then**
  $\Psi_{\text{iso}}^{\max(n)} \leftarrow \Psi_{\text{iso}}^{0,\infty}$ (Loading)
  $\chi \leftarrow 1$
  $\overline{\mathbf{S}}^{\text{r},\infty(n)} \leftarrow -\overline{\mathbf{S}}^{0,\infty}$
else
  $\Psi_{\text{iso}}^{\max(n)} \leftarrow \Psi_{\text{iso}}^{\max(n-1)}$ (Unloading/Reloading)
  $\chi \leftarrow \dfrac{\Psi_{\text{iso}}^{0,\infty}}{\Psi_{\text{iso}}^{\max(n)}}$
  $\overline{\mathbf{S}}^{\text{r},\infty(n)} \leftarrow \overline{\mathbf{S}}^{\text{r},\infty(n-1)}$
end if
Evaluate η_{m} and η_{r} from (2) and $\overline{\mathbf{S}}^{\infty}$ from (5)
for $l = 1$ to M **do**
  $\mathbf{Q}_l^{(n)} \leftarrow \mathcal{H}_l^{(n-1)} + \exp\left(-\dfrac{\Delta t^{(n)}}{2\tau_l}\right) \overline{\mathbf{S}}^{0,\infty(n)}$
  Evaluate $\mathcal{H}_l^{(n)}$ from (9)
end for
Evaluate $\mathbf{Q}$ and $\overline{\mathbf{S}}^{\text{neq}}$ from (6):

$$\begin{aligned}\overline{\mathbf{S}}^{\text{neq}} = \sum_{p\in\{\|,\perp\}} \mu_p [& \gamma_p (\overline{K}_{1p})^{\gamma_p - 1} (\mathbf{H}_p : \mathbf{Q}) \mathbf{H}_p + \\ & + \delta_p (\overline{K}_{-1p})^{\delta_p - 1} (\mathbf{H}'_p : \mathbf{Q}) \mathbf{H}'_p + (\overline{K}_{-1p})^{\delta_p} (\overline{\mathbf{C}}^{-1} \mathbf{Q} \mathbf{H}'_p + \mathbf{H}'_p \mathbf{Q} \overline{\mathbf{C}}^{-1})]\end{aligned}$$

Evaluate $\mathbf{S}$ from (4)
Evaluate the Eulerian stress tensor $\sigma \leftarrow J^{-1} \mathbf{F} \mathbf{S} \mathbf{F}^{\text{T}}$
return $\sigma, \Psi_{\text{iso}}^{\max(n)}, \overline{\mathbf{S}}^{\text{r},\infty(n)}, \mathcal{H}_l^{(n)}$

Finite element procedures based on implicit integration with a Newton-type iterative solution technique require a linearization of the constitutive equations. This is achieved by introducing the fourth-order elasticity tensor defined in the Eulerian setting [38]. Although a closed-form expression can be derived, we have preferred a numerical approximation based on a forward difference scheme introduced by Miehe [44]. Accordingly, the consistent tangent modulus is computed based on a perturbation of the deformation gradient. The method requires N additional evaluations of the

Eulerian stress tensor according to Algorithm 1 with the perturbed deformation gradient, where $N = 4$ for two-dimensional problems and $N = 6$ in three-dimensions. Benchmark tests revealed that the increase in computational time compared to an analytically derived tangent modulus is not significant. The consistent tangent modulus is then obtained as

$$c_{ijkl} = \frac{1}{\epsilon}[\sigma_{ij}(\tilde{\mathbf{F}}^{kl}) - \sigma_{ij}(\mathbf{F})], \tag{10}$$

where ϵ is a perturbation parameter and $\tilde{\mathbf{F}}^{kl}$ is the perturbed deformation gradient obtained by perturbing only its (kl) component. The complete procedure is summarised in the Algorithm 2 reported in the Appendix.

2.2.2. Shell formulation

The constitutive model is adapted to shell elements formulated on the classical Reissner-Mindlin kinematic theory by invoking the plane stress condition, i.e., taking the normal stress in the thickness direction to be zero [45]. The developed plane stress formulation assumes incompressibility $J \equiv 1$ so that the augmented free-energy function in (1) is redefined in the form

$$\Psi = \Psi_{\text{iso}}^{\infty}(\overline{\mathbf{C}}) + \sum_{l=1}^{M} \Upsilon_l(\overline{\mathbf{C}}, \mathbf{\Gamma}_l) - p(J-1), \tag{11}$$

where p is here a Lagrange multiplier computed explicitly by imposing the condition $S_{33} = 0$, i.e. $p = \overline{C}_{33}\mathbf{S}_{\text{iso}}(\overline{\mathbf{C}}) : (\boldsymbol{E}_3 \otimes \boldsymbol{E}_3)$, where $\boldsymbol{E}_3$ identifies the thickness direction in the reference configuration. The stress tensor in (4) is then replaced by

$$\mathbf{S} = \left[\mathbb{I} - \overline{C}_{33}\overline{\mathbf{C}}^{-1} \otimes (\boldsymbol{E}_3 \otimes \boldsymbol{E}_3)\right] : \mathbf{S}_{\text{iso}}(\overline{\mathbf{C}}), \tag{12}$$

where $\mathbf{S}_{\text{iso}} = \overline{\mathbf{S}}^{\infty} + \overline{\mathbf{S}}^{\text{neq}}$ and $\mathbb{I}$ denotes the fourth-order unit tensor defined as $(\mathbb{I})_{IJKL} = (\delta_{IK}\delta_{JL} + \delta_{IL}\delta_{JK})/2$.

2.2.3. Local material orientation

The correct formulation of the proposed constitutive model is based on the definition of the planes of material symmetry. As stated in Section 2, the structure tensors are defined with respect to the orthogonal eigenvector triad $\boldsymbol{E}_i$, $i = 1, 2, 3$. Therefore, the eigenvector base at each material point of the numerical model must be provided in the form of a pair of local reference unit vectors

$\boldsymbol{E}_i$. These can be obtained by transforming the global basis $\boldsymbol{G}_i$ such that $\boldsymbol{E}_i = Q_{ij}\boldsymbol{G}_j$, where $Q_{ij} = \boldsymbol{E}_i \cdot \boldsymbol{G}_j$ is a proper orthogonal tensor [38]. In the current configuration, the local basis follows the rotation of the material point defined by $\mathbf{R}$, where $\mathbf{F} = \mathbf{RU}$ is the polar decomposition of the deformation gradient and $\mathbf{U}$ is the right stretch tensor. The current unit vectors $\boldsymbol{e}_i$ define the so-called corotational basis of the material, with $\boldsymbol{e}_i = R_{ij}\boldsymbol{E}_i$. The corotational formulation is implemented in most commercial FE programs and is useful for practical applications, such as when the local reference basis is aligned with the axial, circumferential, and radial directions of a curvilinear coordinate system. For problems with certain symmetries, as presented in Section 3, the evaluation of the transformation matrix $[\![\mathbf{Q}]\!]$ is straightforward. In more complex cases, the local material orientation can be derived from the solution of multiple auxiliary Laplace problems [46].

3. Representative examples

To show the performance of the numerical model, some selected representative examples are presented in this section. For this purpose, the numerical model was implemented as a user-defined material for the static implicit solver of the commercial FE software Abaqus Standard [35]. All examples assume that the material is perfectly incompressible. Mixed displacement-stress element formulations, with linear interpolation for displacements and constant pressure, are employed.

3.1. Homogeneous deformations

In order to verify the numerical model and to illustrate the physical behavior described by the constitutive framework, we have selected three boundary-value problems. In the case of perfect incompressibility, these can be solved explicitly, since the deformation gradient is completely prescribed, and the unknown Lagrange multiplier p in (11) results from the solution of a system of equations. In the following, the stress-strain curves obtained from a single FE are compared with the analytical solution. We have considered representative material parameters of an electrospun polymeric material (Table 1). Due to confidentiality agreements with the manufacturing company of the polymeric scaffold, Xeltis BV (Eindhoven, The Netherlands), the material parameters and the results shown in this section have been normalised.

The results shown below apply to deformations in the axial-circumferential plane $(\boldsymbol{E}_1, \boldsymbol{E}_2)$. The full set of deformations is reported in the Supplementary Material available online (Figs. 2-4),

183 in addition to another benchmark example to verify the convergence behavior (Supplementary Material, Figs. 5-6).

Material parameter	**Value**
Structure tensor eigenvalue H_{11} (-)	0.55
Structure tensor eigenvalue H_{22} (-)	0.27
Coaxial stiffness $\mu_{\parallel}$ (normalised)	1.00
Coaxial 1st shape parameter $\gamma_{\parallel}$ (-)	1.45
Coaxial 2nd shape parameter $\delta_{\parallel}$ (-)	0.01
Perpendicular stiffness $\mu_{\perp}$ (normalised)	0.21
Perpendicular 1st shape parameter $\gamma_{\perp}$ (-)	2.49
Perpendicular 2nd shape parameter $\delta_{\perp}$ (-)	0.01
Mullins maximum damage parameter $\eta_{\mathrm{m}0}$ (-)	0.78
Mullins damage evolution parameter α_{m} (-)	27.26
Maximum residual stress parameter $\eta_{\mathrm{r}0}$ (-)	0.19
Residual stress evolution parameter α_{r} (-)	2.38
Viscoelastic 1st relaxation time τ_1 (normalised)	1.00
Viscoelastic 1st inverse stiffness ${\mu'_1}^{-1}$ (normalised)	1.54
Viscoelastic 2nd relaxation time τ_2 (normalised)	15.98
Viscoelastic 2nd inverse stiffness ${\mu'_2}^{-1}$ (normalised)	1.31
Viscoelastic 3rd relaxation time τ_3 (normalised)	145.01
Viscoelastic 3rd inverse stiffness ${\mu'_3}^{-1}$ (normalised)	0.44

Table 1. Summary of material parameters for an electrospun polymer for heart valve scaffolds. Stiffness-like quantities are normalised with $\mu_{\parallel}$ and relaxation times with τ_1.

184

185 *3.1.1. Biaxial extension*

186 A biaxial deformation for an incompressible material is prescribed by the following deformation
187 gradient

$$\mathbf{F} = \lambda_1 \boldsymbol{e}_1 \otimes \boldsymbol{E}_1 + \lambda_2 \boldsymbol{e}_2 \otimes \boldsymbol{E}_2 + (\lambda_1 \lambda_2)^{-1} \boldsymbol{e}_3 \otimes \boldsymbol{E}_3, \tag{13}$$

188 where λ_i are the principal stretches and we have assumed that $\boldsymbol{E}_1, \boldsymbol{E}_2$ are the principal material
189 directions aligned with the axes of biaxial extension. Using the plane stress condition (12), the
190 Cauchy stress tensor is given by

$$\boldsymbol{\sigma}(\lambda_1, \lambda_2) = [\mathbb{I} - \mathbf{I} \otimes (\boldsymbol{e}_3 \otimes \boldsymbol{e}_3)] : \boldsymbol{\sigma}_{\mathrm{iso}}(\lambda_1, \lambda_2), \tag{14}$$

191 where $\boldsymbol{\sigma}_{\mathrm{iso}} = \mathbf{F}\mathbf{S}_{\mathrm{iso}}\mathbf{F}^{\mathrm{T}}$.

192 The results are illustrated in Fig. 1(a) for a cyclic loading protocol with two different strain
193 rates and equibiaxial tension $\lambda_1 = \lambda_2 = \lambda$.

3.1.2. *Uniaxial extension*

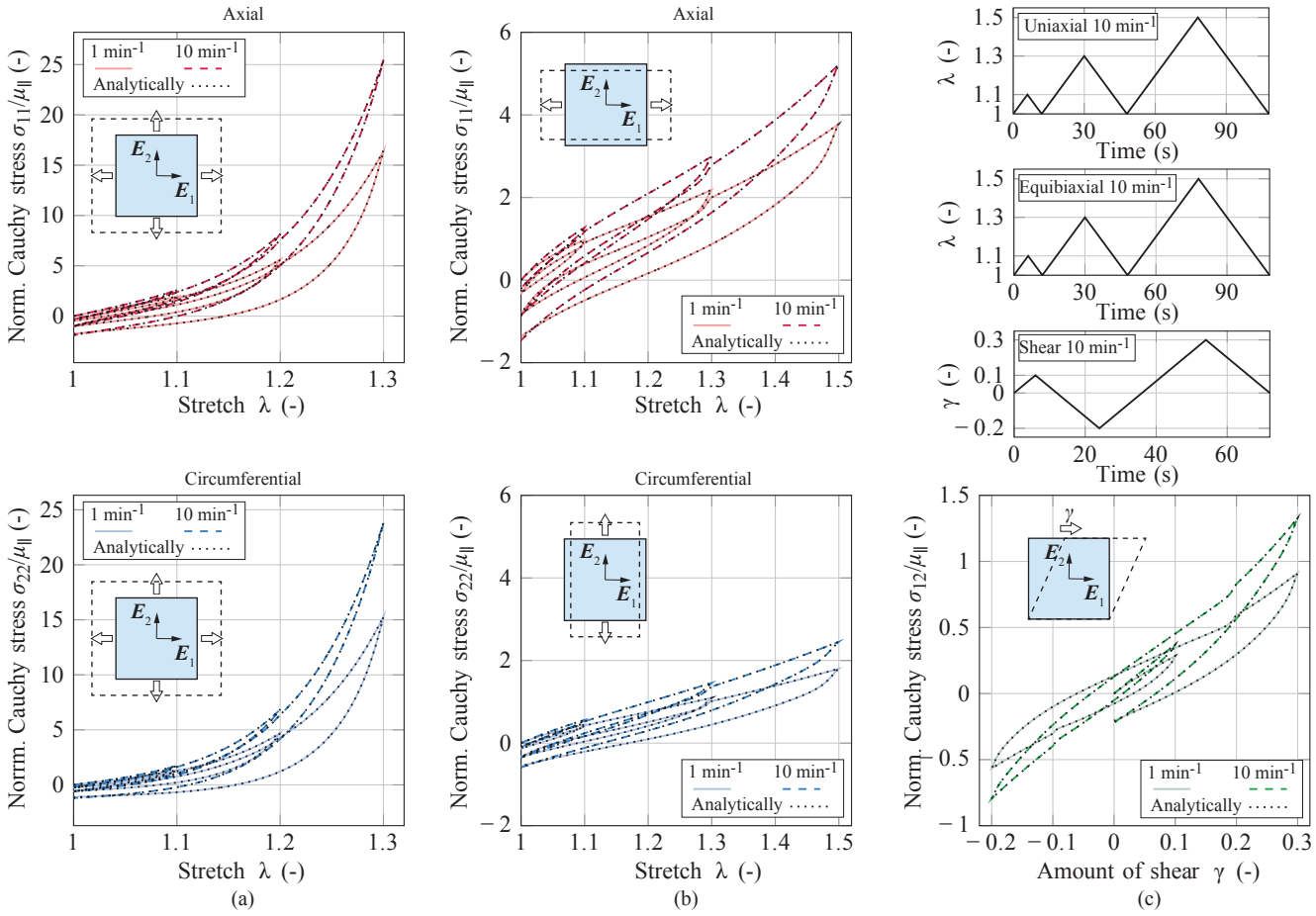

Figure 1. Comparison between analytical and FE solutions for elementary deformations with incompressible behavior. Two strain rates are considered, $1\,\mathrm{min}^{-1}$ and $10\,\mathrm{min}^{-1}$. Cauchy stress versus stretch for (a) equibiaxial extension, (b) uniaxial extension and (c) Cauchy shear stress versus amount of shear for simple shear deformation. The prescribed loading for the higher rate is shown in the top right.

A uniaxial deformation for an incompressible material is defined by the deformation gradient in (13). In addition, we prescribe $\lambda_1 = \lambda$ for a uniaxial extension along the principal direction $\boldsymbol{E}_1$. The Cauchy stress tensor for an anisotropic material is obtained from the solution of

$$\begin{aligned} \boldsymbol{\sigma}(\lambda, \lambda_2) &= [\mathbb{I} - \mathbf{I} \otimes (\boldsymbol{e}_3 \otimes \boldsymbol{e}_3)] : \boldsymbol{\sigma}_{\mathrm{iso}}[\lambda, \lambda_2(\lambda)], \\ &\Longrightarrow \; f : \lambda \to \lambda_2. \end{aligned} \tag{15}$$

A uniaxial extension along the principal direction $\boldsymbol{E}_2$ can be computed analogously, with $\lambda_2 = \lambda$ and $g : \lambda \to \lambda_1$. The results are illustrated in Fig. 1(b).

3.1.3. Simple shear

A simple shear deformation can be prescribed by the following deformation gradient

$$\mathbf{F} = \boldsymbol{e}_1 \otimes \boldsymbol{E}_1 + \boldsymbol{e}_2 \otimes \boldsymbol{E}_2 + \boldsymbol{e}_3 \otimes \boldsymbol{E}_3 + \gamma \boldsymbol{e}_1 \otimes \boldsymbol{E}_2, \tag{16}$$

where γ is the amount of shear along $\boldsymbol{E}_1$. Using the plane stress condition (12), the Cauchy stress tensor is given by

$$\boldsymbol{\sigma}(\gamma) = [\mathbb{I} - \mathbf{I} \otimes (\boldsymbol{e}_3 \otimes \boldsymbol{e}_3)] : \boldsymbol{\sigma}_{\text{iso}}(\gamma). \tag{17}$$

The results are illustrated in Fig. 1(c).

3.2. Parallel plate test validation

The parallel plate test is an experimental procedure commonly used to characterise the elastic and inelastic material response of polymeric materials. In this section, a FE model is developed to simulate this experimental procedure applied to an electrospun polymeric material. This example was selected as a validation of the proposed theoretical and numerical framework. For this purpose, we determined the material parameters of the polymeric material from cyclic uniaxial and biaxial extension tests and stress relaxation experiments. We then employ these parameters in the numerical simulation of the validation experiment. The uncertainty in the experimental measurements was taken into account by developing a probabilistic framework based on Bayesian inference [47], which will be the subject of a follow-up study. Here we focus on the description of the validation experiment and the numerical simulation in which the uncertainty in the experimental data is transferred to the numerical model.

3.2.1. Experimental procedure

We measured the force-displacement curves of two different sample geometries under cyclic compressive loading. The ring-shaped samples were tested in the parallel plate configuration with displacement control at constant velocity. Displacements between 0.25 and 0.75, defined as a fraction of the initial diameter of each sample d_0, were applied. The material was provided by the company Xeltis BV (Eindhoven, The Netherlands) and used as received. To prevent unintended movements during loading and unloading, the samples were fixed at the top and bottom with a thin strip ($d \approx 1\,\text{mm}$) of double-sided adhesive tape. The nominal dimensions of the tested samples and the detailed experimental loading protocols used during work are summarised in Table 2.

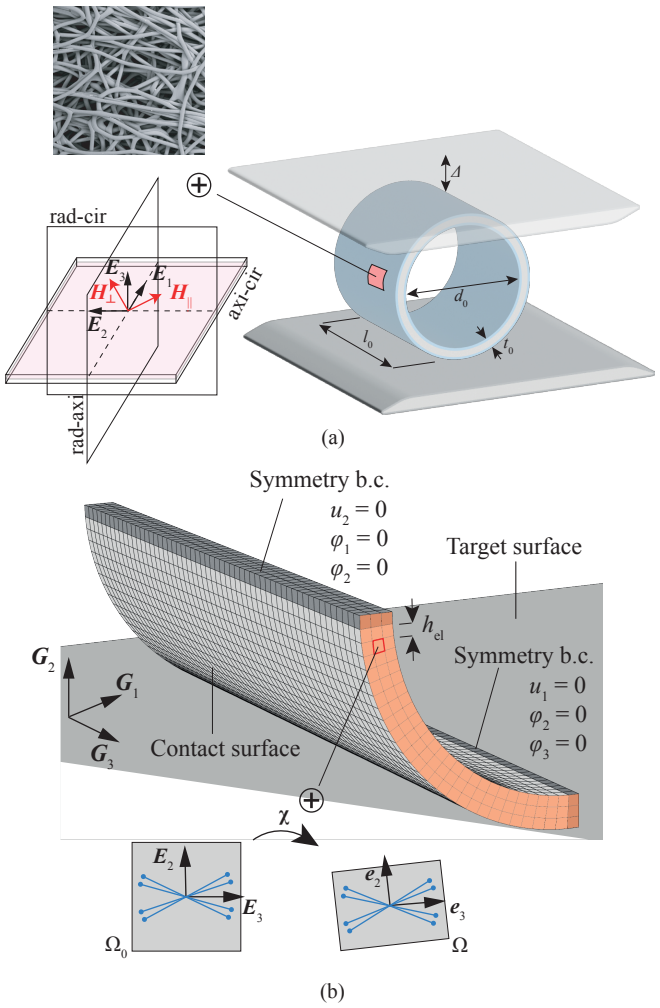

Figure 2. (a) Sketch of the geometry of the parallel plate test showing the planes of material symmetry and a detail of the fibre microstructure (reproduced from [9]). (b) Symmetric FE model with mesh, boundary conditions, contact interactions and local basis. The section of the two-dimensional model is highlighted in red.

All mechanical tests were performed with a displacement-controlled triaxial testing device with a vertical stroke resolution of 0.04 μm [48]. The nominal force of the installed sensor was ± 2 N with an accuracy class of 0.5%. To account for the dispersion in sample lengths (l_0 = 10-16 mm), the recorded forces were normalised to the actual length of each sample for further processing. The original device was modified and updated with a 3D-printed sample stage with a side length of 70 mm. The dimensions of the stage were chosen so large that there is no overhang during testing and to ensure a homogeneous deformation across the whole sample is guaranteed. All tests were performed under dry conditions at room temperature. A total of $n = 6$ samples were tested for each of the two diameters. A scheme of the experimental configuration is shown in Fig. 2(a).

Geometry		
Diameter (internal) d_0	6 mm	23 mm
Thickness t_0	0.5 mm	0.5 mm
Length l_0	10 mm	10 mm
Loading		
Load steps Δ/d_0	0.25-0.50	0.25-0.50-0.75
Loading rate $\dot{\Delta}$	10 mm/min	20 mm/min
Number of cycles	5	5

Table 2. Nominal dimensions and loading protocols of the parallel plate tests.

3.2.2. Finite element model

The FE model is defined by taking advantage of the double symmetry of the problem such that only a quarter of the geometry is modelled as a three-dimensional deformable body. A local cylindrical reference system is defined by the orthogonal basis $(\boldsymbol{E}_i)_{i=1}^3$, where $\boldsymbol{E}_1, \boldsymbol{E}_2$ indicate the axial and circumferential direction, respectively. The metal plate is defined as an analytical surface and is associated with a rigid body reference node. Then, a contact interaction between the analytical surface, which acts as the target, and the outer surface of the cylinder, which acts as the contact, is defined using the contact pair algorithm of Abaqus Standard FE solver with surface-to-surface contact discretization. Contact properties are defined by a frictionless canonical pressure-overclosure relationship. The effect of glue between plate and specimen is simulated by imposing a non-separation behavior on a strip with a width approximately equal to the width of the tape used in the experiments. This specification prevents nodes from loosening after contact and thus creating tensile forces during unloading. Boundary conditions are defined to prevent rigid body motion and enforce symmetry. The loading is assigned by imposing a vertical displacement on the rigid body reference node while constraining all other degrees of freedom and using an amplitude curve to define the loading history as in the experimental protocol. A sketch of the reference configuration of the FE model is shown in Fig. 2(b). A preliminary mesh convergence study is performed by tracking the resultant force and maximum true principal strain at the largest diameter. The optimal mesh has a relative characteristic element size of $h_{\mathrm{el}}/d_0 = 0.03$ and $h_{\mathrm{el}}/d_0 = 0.01$ for $d_0 = 6\,\mathrm{mm}$ and $d_0 = 23\,\mathrm{mm}$, respectively.

In order to validate the numerical model with the experiments, uncertainties related to the experimental geometries should also be considered. For the diameter of the cylindrical sample we have assumed a uniform distribution within the limits $d_0 \pm 1\,\mathrm{mm}$. It was assumed that the thickness follows a normal distribution with a mean of t_0 and a standard deviation of 0.01 mm (Ta-

ble 2). A total of 800 simulations were run for each diameter, randomly selecting geometric and material properties from the specified distributions. In order to reduce the computational time, a plane strain assumption in the axial direction was introduced, so that a two-dimensional model is obtained in the circumferential-radial plane ($\boldsymbol{E}_2, \boldsymbol{E}_3$) (see Fig. 2(b)). A comparison between representative three-dimensional and plane strain solutions is reported in the Supplementary Material available online (Fig. 7). Representative results of the simulations with the diameter $d_0 = 23\,\mathrm{mm}$

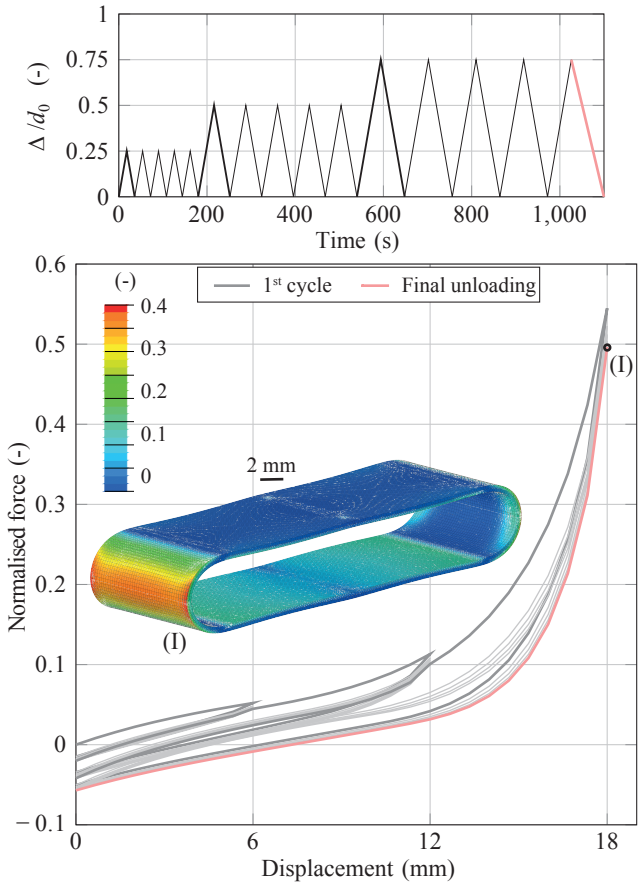

Figure 3. Normalised force-displacement curve from the parallel plate test simulation with diameter 23 mm (compressive forces are positive). The loading protocol is shown on top. The inset shows contours of the maximum principal Cauchy stress at the point of maximal compression normalised by $\mu_\parallel$.

are shown in Fig. 3, where the material parameters given in Table 1 were used with mean geometric values. The normalised reaction force $\bar{F} = F/(\mu_\parallel d_0)$ and the prescribed displacement were extracted from the reference node of the rigid plate and doubled to account for symmetry. Figure 4 shows the comparison with the experimental results, using only the data from the last unloading curve of the last loading step. The FE result is represented by the median within a 90% confidence interval. The experimental results are visualised as a mean along with the maximum and minimum measurements. The corresponding plots for the diameter $d_0 = 6\,\mathrm{mm}$ can be found

in the Supplementary Material available online (Fig. 9).

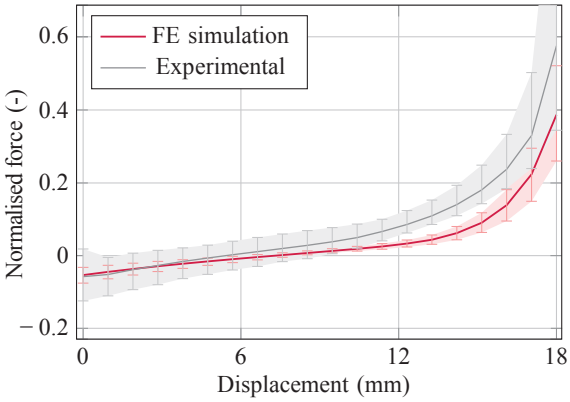

Figure 4. Comparison of parallel plate test simulation with experimental results for a diameter of 23 mm (compressive forces are positive).

4. Discussion

Polymeric scaffolds have received increased popularity in tissue engineering because of the innovative design paradigm they have introduced. However, the full potential of the *in situ* tissue engineering approach is still hampered by the large number of design variables that can potentially affect the final outcome in terms of functionality and safety of the replacement implant. In our research we focused on the mechanical behavior of the scaffold material prior to the degradation process and native tissue formation.

The new constitutive model [32] recently introduced by the authors encompasses the full set of nonlinear and inelastic effects observed in typical electrospun polymers used for the scaffolds in a continuum mechanics framework. As a further and fundamental step, we have proposed an efficient numerical implementation of the model for the FE method in this work. The code was developed for the commercial software Abaqus and can be adapted to other commercial FE packages, allowing a straightforward use in the biomedical industry. In addition, the numerical implementation was verified by comparing the FE results with semi-analytical solutions for elementary deformations and validated through a large scale bending problem with contact.

The verification tasks were successfully completed, demonstrating the correctness of the numerical implementation. Overall, the constitutive behavior observed in response to elementary deformations indicates a strongly anisotropic response of the scaffold material in the local axial-circumferential plane (Fig. 1). Furthermore, the expected rate-stiffening effect is also correctly

captured by the model.

The validation problem was selected to allow large-scale application of the model. Furthermore, additional complexity is introduced by the kinematic nonlinearities arising from contact interactions. Qualitatively, the simulation can reproduce the large hysteresis in the force-displacement curves and the different features observed between the two experimental geometries. The quantitative comparison is also satisfactory (Fig. 4), although there are some differences worth discussing. First, the selected example is very sensitive to geometrical effects. As a rough measure of the influence, the reaction force when bending a circular ring scales into the linear elasticity with the third power of the thickness [49]. For this reason, we included a quantification of the uncertainties on the experimental geometry in the simulation. In addition, the different boundary-value problem of the validation with regard to material parameter identification could also explain part of the observed discrepancy. Material parameters were identified using elementary uniaxial and biaxial deformations with stretches up to fifty percent, but no experiment was specifically designed to test the compressive response of the material. On the contrary, the validation problem involves extensive compression, very large displacements, but only moderate deformations (Fig. 8 in the Supplementary Material available online). These observations underscore the importance of an appropriate selection of experimental protocols, a constitutive modelling framework and a validation problem in the development of biomedical solutions. Despite the limitations, the proposed constitutive model and its numerical implementation show great potential for more complex simulations in the future.

Appendix A. Consistent Eulerian tangent modulus

The method summarised in Algorithm 2 evaluates the consistent Eulerian tangent modulus for integration schemes developed in a corotational formulation based on the Jaumann rate of the Kirchoff stress [50]. The elasticity tensor in (10) is here computed in matrix form using the Voigt notation for fourth-order tensors with minor symmetries, although the final matrix for this particular constitutive model is non-symmetric in general.

Algorithm 2 Computation of the Eulerian tangent modulus[1]

Given $\Delta t^{(n)}, \mathbf{F}^{(n)}, \Psi_{\text{iso}}^{\max(n-1)}, \overline{\mathbf{S}}^{\text{r},\infty(n-1)}, \mathcal{H}_l^{(n-1)}, \epsilon$
Evaluate $\boldsymbol{\sigma}$ with Algorithm 1 for $\mathbf{F}^{(n)}$
Define Voigt's lookup table:
  LUT $\leftarrow ((1,1),(2,2),(3,3),(1,2),(1,3),(2,3))$
Form local Eulerian base $\boldsymbol{e}_i, i = 1,2,3$
for $B = 1$ to 6 **do**
  k, $m \leftarrow$ LUT$[B]$
  $\boldsymbol{e}_k$, $\boldsymbol{e}_m \leftarrow$ base$[k]$, base$[m]$
  $\Delta\mathbf{F} \leftarrow \frac{\epsilon}{2}\left(\boldsymbol{e}_k \otimes \boldsymbol{e}_m \mathbf{F}^{(n)} + \boldsymbol{e}_m \otimes \boldsymbol{e}_k \mathbf{F}^{(n)}\right)$
  Compute $\tilde{\mathbf{F}}^{(n)} \leftarrow \mathbf{F}^{(n)} + \Delta\mathbf{F}$
  Evaluate $\tilde{\boldsymbol{\sigma}}$ with Algorithm 1 for $\tilde{\mathbf{F}}^{(n)}$
  for $A = 1$ to 6 **do**
    i, $j \leftarrow$ LUT$[A]$
    $[c]_{A,B} \leftarrow \frac{1}{\epsilon}\left(\tilde{\sigma}_{ij} - \sigma_{ij}\right)$
  end for
end for
return $[c]$

[1] History variables are not updated during the perturbation step.

Author Contributions

M.T.: Conceptualisation, Formal Analysis, Methodology, Software, Visualisation, Writing – original draft; M.P.W.: Conceptualisation, Formal Analysis, Methodology, Writing – review and editing; M.P.K.: Investigation, Methodology, Writing – original draft; M.R.: Methodology, Project administration, Writing – review and editing; N.G.: Project administration, Resources; G.A.H.: Funding acquisition, Methodology, Supervision, Writing – review and editing.

Acknowledgements

We thank Christina Bachmayer (Graz University of Technology, Institute of Biomechanics) for her contribution in the experimental work.

Data Accessibility

The source code of the Abaqus Standard user-material subroutine is available from: https://doi.org/10.3217/bhxxe-ng262. Additional derivations and results can be found in the Supplementary Material available online.

Funding

We gratefully acknowledge the financial support provided by the European Union's Horizon 2020 program for research and innovation under grant agreement no. 101017523.

References

[1] M. S. Sacks, A. P. Yoganathan, Heart valve function: a biomechanical perspective, Philosophical Transactions of the Royal Society B: Biological Sciences 362 (2007) 1369–1391. doi:10.1098/rstb.2007.2122.

[2] A. Cribier, H. Eltchaninoff, A. Bash, N. Borenstein, C. Tron, F. Bauer, G. Derumeaux, F. Anselme, F. Laborde, M. B. Leon, Percutaneous transcatheter implantation of an aortic valve prosthesis for calcific aortic stenosis, Circulation 106 (2002) 3006–3008. doi:10.1161/01.CIR.0000047200.36165.B8.

[3] A. Mol, A. I. P. M. Smits, C. V. C. Bouten, F. P. T. Baaijens, Tissue engineering of heart valves: advances and current challenges, Expert Review of Medical Devices 6 (2009) 259–275. doi:10.1586/erd.09.12.

[4] T. B. Wissing, V. Bonito, C. V. C. Bouten, A. I. P. M. Smits, Biomaterial-driven in situ cardiovascular tissue engineering—a multi-disciplinary perspective, npj Regenerative Medicine 2 (2017) 18. doi:10.1038/s41536-017-0023-2.

[5] J. Kluin, H. Talacua, A. I. P. M. Smits, M. Y. Emmert, M. C. P. Brugmans, E. S. Fioretta, P. E. Dijkman, S. H. M. Söntjens, R. Duijvelshoff, S. Dekker, M. W. J. T. Janssen-van den Broek, V. Lintas, A. Vink, S. P. Hoerstrup, H. M. Janssen, P. Y. W. Dankers, F. P. T. Baaijens, C. V. C. Bouten, In situ heart valve tissue engineering using a bioresorbable elastomeric implant – from material design to 12 months follow-up in sheep, Biomaterials 125 (2017) 101–117. doi:10.1016/j.biomaterials.2017.02.007.

[6] A. H. Chester, J. K. Grande-Allen, Which biological properties of heart valves are relevant to tissue engineering?, Frontiers in Cardiovascular Medicine 7 (2020). doi:10.3389/fcvm.2020.00063.

[7] E. S. Fioretta, S. E. Motta, V. Lintas, S. Loerakker, K. K. Parker, F. P. T. Baaijens, V. Falk, S. P. Hoerstrup, M. Y. Emmert, Next-generation tissue-engineered heart valves with repair, remodelling and regeneration capacity, Nature Reviews Cardiology 18 (2021) 92–116. doi:10.1038/s41569-020-0422-8.

[8] B. J. De Kort, J. Marzi, E. M. Brauchle, A. M. Lichauco, H. S. Bauer, A. Serrero, S. Dekker, M. A. J. Cox, F. J. Schoen, K. Schenke-Layland, C. V. C. Bouten, A. I. P. M. Smits, Inflammatory and regenerative processes in bioresorbable synthetic pulmonary valves up to two years in sheep–spatiotemporal insights augmented by raman microspectroscopy, Acta Biomaterialia 135 (2021) 243–259. doi:10.1016/j.actbio.2021.09.005.

[9] L. A. Bockeria, O. Svanidze, A. Kim, K. Shatalov, V. Makarenko, M. Cox, T. Carrel, Total cavopulmonary connection with a new bioabsorbable vascular graft: First clinical experience, The Journal of Thoracic and Cardiovascular Surgery 153 (2017) 1542–1550. doi:10.1016/j.jtcvs.2016.11.071.

[10] D. L. Morales, C. Herrington, E. A. Bacha, V. O. Morell, Z. Prodán, T. Mroczek, S. Sivalingam, M. Cox, G. Bennink, F. M. Asch, A novel restorative pulmonary valve conduit: Early outcomes of two clinical trials, Frontiers in Cardiovascular Medicine 7 (2021) 1–9. doi:10.3389/fcvm.2020.583360.

[11] J. D. Humphrey, Cardiovascular Solid Mechanics: Cells, Tissues, and Organs, Springer, 2002.

[12] T. Courtney, M. S. Sacks, J. Stankus, J. Guan, W. Wagner, Design and analysis of tissue engineering scaffolds that mimic soft tissue mechanical anisotropy, Biomaterials 27 (2006) 3631–3638. doi:10.1016/j.biomaterials.2006.02.024.

[13] N. J. B. Driessen, R. A. Boerboom, J. M. Huyghe, C. V. C. Bouten, F. P. T. Baaijens, Computational analyses of mechanically induced collagen fiber remodeling in the aortic heart valve, Journal of Biomechanical Engineering 125 (2003) 549–557. doi:10.1115/1.1590361.

[14] B. M. Baker, N. L. Nerurkar, J. A. Burdick, D. M. Elliott, R. L. Mauck, Fabrication and modeling of dynamic multipolymer nanofibrous scaffolds, Journal of Biomechanical Engineering 131 (2009) 1–10. doi:10.1115/1.3192140.

[15] D. Li, Y. Xia, Electrospinning of nanofibers: Reinventing the wheel?, Advanced Materials 16 (2004) 1151–1170. doi:10.1002/adma.200400719.

[16] Q. P. Pham, U. Sharma, A. G. Mikos, Electrospinning of polymeric nanofibers for tissue engineering applications: A review, Tissue Engineering 12 (2006) 1197–1211. doi:10.1089/ten.2006.12.1197.

[17] S. Loerakker, T. Ristori, F. P. T. Baaijens, A computational analysis of cell-mediated compaction and collagen remodeling in tissue-engineered heart valves, Journal of the Mechanical Behavior of Biomedical Materials 58 (2016) 173–187. doi:10.1016/j.jmbbm.2015.10.001.

[18] M. Y. Emmert, B. A. Schmitt, S. Loerakker, B. Sanders, H. Spriestersbach, E. S. Fioretta, L. Bruder, K. Brakmann, S. E. Motta, V. Lintas, P. E. Dijkman, L. Frese, F. Berger, F. P. T. Baaijens, S. P. Hoerstrup, Computational modeling guides tissue-engineered heart valve design for long-term in vivo performance in a translational sheep model, Science Translational Medicine 10 (2018). doi:10.1126/scitranslmed.aan4587.

[19] S. Loerakker, J. D. Humphrey, Computer model-driven design in cardiovascular regenerative medicine, Annals of Biomedical Engineering (2022). doi:10.1007/s10439-022-03037-5.

[20] K. S. Miller, Y. U. Lee, Y. Naito, C. K. Breuer, J. D. Humphrey, Computational model of the in vivo development of a tissue engineered vein from an implanted polymeric construct, Journal of Biomechanics 47 (2014) 2080–2087. doi:10.1016/j.jbiomech.2013.10.009.

[21] N. Famaey, J. Vastmans, H. Fehervary, L. Maes, E. Vanderveken, F. Rega, S. J. Mousavi, S. Avril, Numerical simulation of arterial remodeling in pulmonary autografts, ZAMM Zeitschrift fur Angewandte Mathematik und Mechanik 98 (2018) 2239–2257. doi:10.1002/zamm.201700351.

[22] J. D. Drews, V. K. Pepper, C. A. Best, J. M. Szafron, J. P. Cheatham, A. R. Yates, K. N. Hor, J. C. Zbinden, Y. C. Chang, G. J. M. Mirhaidari, A. B. Ramachandra, S. Miyamoto, K. M. Blum, E. A. Onwuka, J. Zakko, J. Kelly, S. L. Cheatham, N. King, J. W. Reinhardt, T. Sugiura, H. Miyachi, Y. Matsuzaki, J. Breuer, E. D. Heuer, T. A. West, T. Shoji, D. Berman, B. A. Boe, J. Asnes, M. Galantowicz, G. Matsumura, N. Hibino, A. L. Marsden, J. S. Pober, J. D. Humphrey, T. Shinoka, C. K. Breuer, Spontaneous reversal of

stenosis in tissue-engineered vascular grafts, Science Translational Medicine 12 (2020) 1–14. doi:10.1126/scitranslmed.aax6919.

[23] M. Latorre, J. M. Szafron, A. B. Ramachandra, J. D. Humphrey, In vivo development of tissue engineered vascular grafts: a fluid-solid-growth model, Biomechanics and Modeling in Mechanobiology 21 (2022) 1–22. doi:10.1007/s10237-022-01562-9.

[24] G. A. Holzapfel, T. C. Gasser, R. W. Ogden, A new constitutive framework for arterial wall mechanics and a comparative study of material models, Journal of Elasticity 61 (2000) 1–48. doi:10.1023/A:1010835316564.

[25] B. Pierrat, V. Nováček, S. Avril, F. Turquier, Mechanical characterization and modeling of knitted textile implants with permanent set, Journal of the Mechanical Behavior of Biomedical Materials 114 (2021) 104210. doi:10.1016/j.jmbbm.2020.104210.

[26] X. Xu, H. Yan, C. Xiao, H. Yao, An anisotropic hyper-visco-pseudo-elastic model and explicit stress solutions for fabric reinforced rubber composites, International Journal of Solids and Structures 242 (2022) 111519. doi:10.1016/j.ijsolstr.2022.111519.

[27] D. A. Head, A. J. Levine, F. C. MacKintosh, Distinct regimes of elastic response and deformation modes of cross-linked cytoskeletal and semiflexible polymer networks, Physical Review E 68 (2003) 061907. doi:10.1103/PhysRevE.68.061907.

[28] N. L. Nerurkar, R. L. S. Mauck, D. M. Elliott, Modeling interlamellar interactions in angle-ply biologic laminates for annulus fibrosus tissue engineering, Biomechanics and Modeling in Mechanobiology 10 (2011) 973–984. doi:10.1007/s10237-011-0288-0.

[29] S. Domaschke, M. Zündel, E. Mazza, A. E. Ehret, A 3D computational model of electrospun networks and its application to inform a reduced modelling approach, International Journal of Solids and Structures 158 (2019) 76–89. doi:10.1016/j.ijsolstr.2018.08.030.

[30] R. L. Li, J. Russ, C. Paschalides, G. Ferrari, H. Waisman, J. W. Kysar, D. Kalfa, Mechanical considerations for polymeric heart valve development: Biomechanics, materials, design and manufacturing, Biomaterials 225 (2019) 119493. doi:10.1016/j.biomaterials.2019.119493.

[31] A. Anssari-Benam, Y.-T. Tseng, G. A. Holzapfel, A. Bucchi, Rate-dependent mechanical behaviour of semilunar valves under biaxial deformation: From quasi-static to physiological

loading rates, Journal of the Mechanical Behavior of Biomedical Materials 104 (2020) 103645. doi:10.1016/j.jmbbm.2020.103645.

[32] M. P. Wollner, M. Terzano, M. Rolf-Pissarczyk, G. A. Holzapfel, A general model for anisotropic pseudo-elasticity and viscoelasticity at large strains, Journal of the Mechanics and Physics of Solids (2023) 105403. doi:10.1016/j.jmps.2023.105403.

[33] A. S. of Mechanical Engineers. Standard for Verification, V. in Computational Fluid Dynamics, H. T. A. V. 20, The American Society of Mechanical Engineers (ASME), 2009.

[34] A. S. of Mechanical Engineers. Assessing Credibility of Computational Modeling through Verification, V. A. to Medical Devices-VV40-2018, ASME V&V40-2018, 2018.

[35] Dassault Systèmes SIMULIA, Abaqus 2018, Documentation, 2018.

[36] J. C. Simo, On a fully three-dimensional finite-strain viscoelastic damage model: Formulation and computational aspects, Computer Methods in Applied Mechanics and Engineering 60 (1987) 153–173. doi:10.1016/0045-7825(87)90107-1.

[37] G. A. Holzapfel, T. C. Gasser, A viscoelastic model for fiber-reinforced composites at finite strains: Continuum basis, computational aspects and applications, Computer Methods in Applied Mechanics and Engineering 190 (2001) 4379–4403. doi:10.1016/S0045-7825(00)00323-6.

[38] G. A. Holzapfel, Nonlinear Solid Mechanics: A Continuum Approach for Engineering Science, Wiley, 2000.

[39] J. Liu, M. Latorre, A. L. Marsden, A continuum and computational framework for viscoelastodynamics: I. finite deformation linear models, Computer Methods in Applied Mechanics and Engineering 385 (2021) 114059. doi:10.1016/j.cma.2021.114059.

[40] C. Miehe, J. Keck, Superimposed finite elastic–viscoelastic–plastoelastic stress response with damage in filled rubbery polymers. experiments, modelling and algorithmic implementation, Journal of the Mechanics and Physics of Solids 48 (2000) 323–365. doi:10.1016/S0022-5096(99)00017-4.

[41] R. W. Ogden, D. G. Roxburgh, A pseudo-elastic model for the mullins effect in filled rubber, Proceedings of the Royal Society A: Mathematical, Physical and Engineering Sciences 455 (1999) 2861–77. doi:10.1098/rspa.1999.0431.

[42] C. Naumann, J. Ihlemann, On the thermodynamics of pseudo-elastic material models which reproduce the mullins effect, International Journal of Solids and Structures 69-70 (2015) 360–369. doi:10.1016/j.ijsolstr.2015.05.014.

[43] J. Schröder, P. Neff, V. Ebbing, Anisotropic polyconvex energies on the basis of crystallographic motivated structural tensors, Journal of the Mechanics and Physics of Solids 56 (2008) 3486–3506. doi:10.1016/j.jmps.2008.08.008.

[44] C. Miehe, Numerical computation of algorithmic (consistent) tangent moduli in large-strain computational inelasticity, Computer Methods in Applied Mechanics and Engineering 134 (1996) 223–240. doi:10.1016/0045-7825(96)01019-5.

[45] S. Klinkel, S. Govindjee, Using finite strain 3D-material models in beam and shell elements, Engineering Computations 19 (2002) 254–271. doi:10.1108/02644400210423918.

[46] R. Schussnig, D. R. Pacheco, M. Kaltenbacher, T. P. Fries, Semi-implicit fluid–structure interaction in biomedical applications, Computer Methods in Applied Mechanics and Engineering 400 (2022) 115489. doi:10.1016/j.cma.2022.115489.

[47] S. Ranftl, T. S. Müller, U. Windberger, G. Brenn, W. von der Linden, A Bayesian approach to blood rheological uncertainties in aortic hemodynamics, International Journal for Numerical Methods in Biomedical Engineering (2023). doi:10.1002/cnm.3576.

[48] G. Sommer, M. Eder, L. Kovacs, H. Pathak, L. Bonitz, C. Mueller, P. Regitnig, G. A. Holzapfel, Multiaxial mechanical properties and constitutive modeling of human adipose tissue: A basis for preoperative simulations in plastic and reconstructive surgery, Acta Biomaterialia 9 (2013) 9036–9048. doi:https://doi.org/10.1016/j.actbio.2013.06.011.

[49] S. Timoshenko, J. Gere, Theory of Elastic Stability, second ed., McGraw-Hill, 1963.

[50] W. Sun, E. L. Chaikof, M. E. Levenston, Numerical approximation of tangent moduli for finite element implementations of nonlinear hyperelastic material models, Journal of Biomechanical Engineering 130 (2008) 1–7. doi:10.1115/1.2979872.